

Study on overlap rate and machinability of selected laser melting of maraging steel

Zeyu Yang*, Weimin Li, Shufen Liu, Qi Gao

School of Mechanical Engineering and Automation, Liaoning University of Technology, Jinzhou Liaoning 121001, China

In order to investigate the material properties of maraging steel laser additive manufacturing, the cladding layers with different overlap rates on the surface of 18Ni300 were prepared by laser cladding technology, and the morphology, microstructure, and hardness of the cladding layer with different overlap rates were analyzed by various means. The results show that the macroscopic morphology of the cladding layer mainly presents three states under different overlap rates, and the change of overlap rate has no effect on the microstructure in the same area of the cladding layer, but does have an effect on the size of the cladding layer. In the end, the optimum overlap rate is 50%, the surface is smooth, the inner is free from defects, the bonding effect is good, and the metallographic structure is even with high hardness. Milling experiments were carried out on the material after laser additive manufacturing, and the surface morphology was observed, confirming a smooth and well-flattened surface with a roughness of $0.342 \mu\text{m}$ had been obtained. The suitable overlap rate can make the coating surface smoother, reduce the subsequent processing loss, and improve the production efficiency and powder utilization rate while ensuring the coating quality.

Keywords: *laser cladding, overlap rate, 18Ni300, surface topography*

1. Introduction

In the past decade, the rapid development of additive manufacturing has shifted its focus to industrial applications and soon after to metal processing [1]. Laser cladding is the most common additive manufacturing process, and it has been widely used in many fields [2]. However, in the process of laser cladding, because of the complex forming process, the cladding layer is prone to cracking [3, 4], porosity [5, 6], and other defects, which is not conducive to building the desired mechanical properties of the material. 18Ni300 is a typical maraging steel with the advantages of high strength, good toughness and small thermal deformation. It is widely used in precision moulds, aerospace, national defense and other engineering applications [7].

The material properties of maraging steels are well suited to the laser powder bed fusion process to produce parts that require excellent strength, hardness, and thermal stability, making 18Ni300

maraging steel suitable for additive manufacturing [8]. Using different directions and methods, a large number of scholars have also carried out research on 18Ni300: Sung et al. [9] used selective laser melting (SLM) to prepare volume cubic 18Ni300 maraging steel and studied the relationship between macro- and micro-mechanical properties and process parameters. It provides a reference for the SLM process of 18Ni300 maraging steel. Yan et al. [10] studied the effect of SLM on the microstructure and mechanical properties of 18Ni300 maraging steel. With the increase of laser power, the grain size of the cladding layer decreases, and the microstructure becomes compact. Bai et al. [11] investigated the effects of laser power, scanning speed, gap spacing, and layer thickness on pool morphology, surface quality, and inner hole defects in 18Ni300 maraging steel. Mei et al. [12] studied the microstructure evolution of 18Ni300 prepared by L-PBF at different scales with aging temperatures. Some important problems, such as the change of metallographic structure, were evaluated, and high-performance materials were prepared. Li et al. [13] studied the

* E-mail: 1552613466@qq.com

mechanism and mechanical properties of 18Ni300 maraging steel formed by SLM. The fracture mode of the tensile specimen is a mixed fracture of brittleness and toughness.

For surface modification of materials and repair of large, damaged areas of parts, the only way to achieve relatively large areas is by multi-pass laser cladding. A suitable lap rate results in a flatter coating surface and reduces subsequent processing losses. But for the 18Ni300 maraging steel of SLM, most of them also focus on the optimization of process parameters and heat treatment. In addition, SLM manufacturing parts of poor surface accuracy also limit the application [14]. These defects can affect corrosion resistance [15], friction performance [16], fatigue life [17], and so on. In this regard, in order to improve the service life of the material and reduce the material failure caused by defects, the 18Ni300 cladding layer was prepared by laser cladding on 18Ni300 substrate, and the morphology, organization, and hardness of the cladding layer of 18Ni300 maraging steel were observed and analyzed by different overlap rates. Finally, milling experiments were carried out. This paper provides a reference for material surface additive manufacturing and re-machining, which is favorable for practical application.

2. Experimental method

2.1. Experimental materials

In this experiment, Vilory New Material Technology Co. vacuum-atomized 18Ni300 powder and rolled 18Ni300 substrate were used. The elemental composition of the powder is shown in Table 1. The powder's appearance is shown in Figure 1, with a particle size of 45–105 μm . Before the experiment, the substrate was polished to prevent surface impurities and the oxide layer from affecting the experiment, and the powder was dried to remove moisture. After the experiment, the material was

Table 1. Elemental composition of 18Ni300 powder

Ni	Co	Mo	Ti	Al	Cr	P	Mn	Si	C	S
18.3	8.9	4.7	0.7	0.2	0.1	0.05	0.02	0.03	0.05	0.03

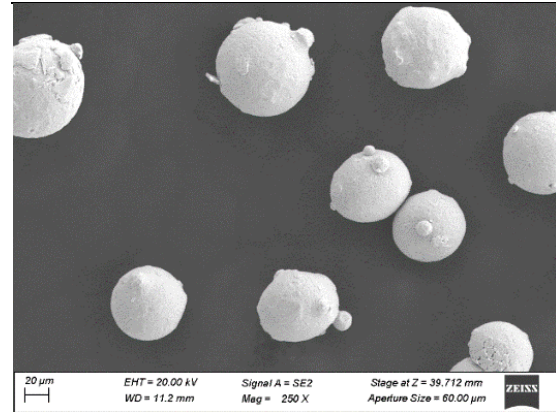


Fig. 1. 18Ni300 powder microstructure

cut into convenient polishing shape using wire-cutting technology, and the cladding layer was polished many times with 600–2000 mesh sandpaper, then polished with metallographic grinding and polishing tester and grinding paste. The surface of the polished cladding layer was etched with aqua regia, and the surface was cleaned and dried with industrial alcohol.

2.2. Laser additive manufacturing process

The equipment used for laser additive manufacturing is the YLK-3000 fiber laser integrated processing system, which consists of the YLR-3000 high-power fiber laser; the large-load, high-precision programmable KUKA-KR30H 6-axis robot; the PERCITEC YC52 laser cladding head with four coaxial powder feeding channels, a cooling water channel, a protective gas channel, and the FHPF-10 synchronous dual-channel powder feeder, synchronized dual-channel powder feeder, and other equipment. During the experiment, the powder is driven by the powder-feeding gas through the synchronous powder-feeding device. The powder is shot out from the powder-spraying orifice on the laser cladding head to the substrate, and at the same time, it interacts with the high-energy laser beam to form the molten pool. As the KUKA Robot moves along a pre-programmed path, the desired cladding coating is eventually formed. The experimental embodiment is shown in Figure 2, where helium gas is used as a protective gas in the additive manufacturing

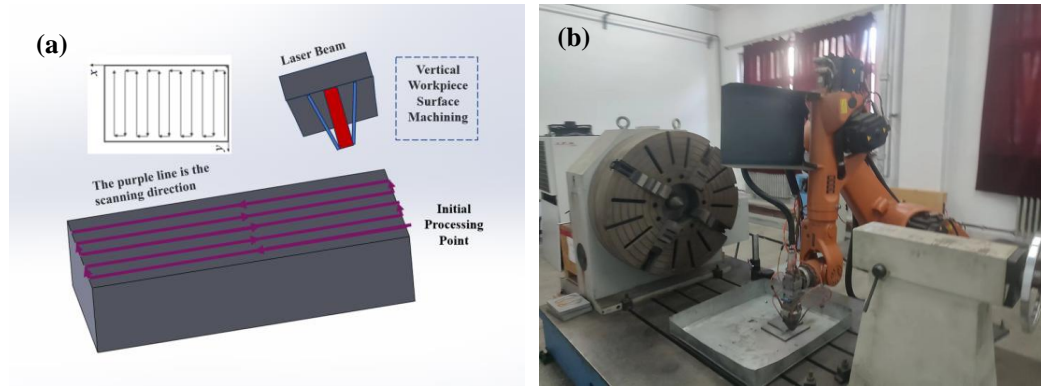


Fig. 2. Experimental implementation plan: (a) experiment design path scheme; (b) additive material manufacturing work platform

Table 2. Experimental process parameters of additive manufacturing

Laser power W	Scan speed mm/s	Speed of power feeding g/min
1300	2	10

process. Based on the previous research, the experimental parameters of additive manufacturing are shown in Table 2.

Overlap rate is the degree of overlap between adjacent cladding channels in laser cladding. A change of overlap rate will directly affect the shape and performance of the workpiece after cladding, and a suitable overlap rate can make the material produced more compact [18]. An overlap rate that is too large or too small will have a negative effect, as shown in Figure 3(a). Here, the overlap rate is too low, the surface of the cladding layer is “wavy,” and there is a significant depression between the adjacent fusion channel. The surface smoothness of the cladding layer is poor, and cracks are appear easily between the melt channels, so the quality of the cladding layer will be affected by further processing. Figure 3(b) shows a moderate overlap rate: a flat surface is formed between adjacent melt paths, and the surface flatness is good, which is an ideal overlap rate for subsequent treatment. Figure 3(c) shows that if the overlap rate is too high, the melt channels overlap each other. Under these circumstances, the cladding layer will increase continuously with further processing, the

change of the defocus of laser cladding may result in a change of the surface morphology and internal structure of the cladding layer. In Figure 3(d), H is the height of the cladding layer, h is the depth of the cladding layer, R is the overlap rate, D_0 is the lap width, and W is the single channel width. The calculation of overlap rate can be simplified as the ratio of the overlap width D_0 between adjacent cladding tracks and the width W of a single cladding layer in multi-pass laser cladding [19], which can be simplified as equation (1).

$$R = D_0/W \quad (1)$$

First, a single-layer, single-track laser cladding experiment is carried out, the height and width of the experimental results are measured, and the lap ratio is calculated with equation (1). According to previous investigations [20–22], most of the studies on the overlap rate are in the range of 30% to 70%, and our research is based on this range of experiments.

2.3. Processing

In this research, the material produced by laser additive manufacturing is processed by milling. The cutting tool is a double-edged end mill with a diameter of 0.8 mm, and the cutting mode is dry cutting. The manufacturing equipment uses the Carver 400GA CNC precision machine tool. The experimental parameters were obtained from the 18Ni300 material processing line of the Wuxi

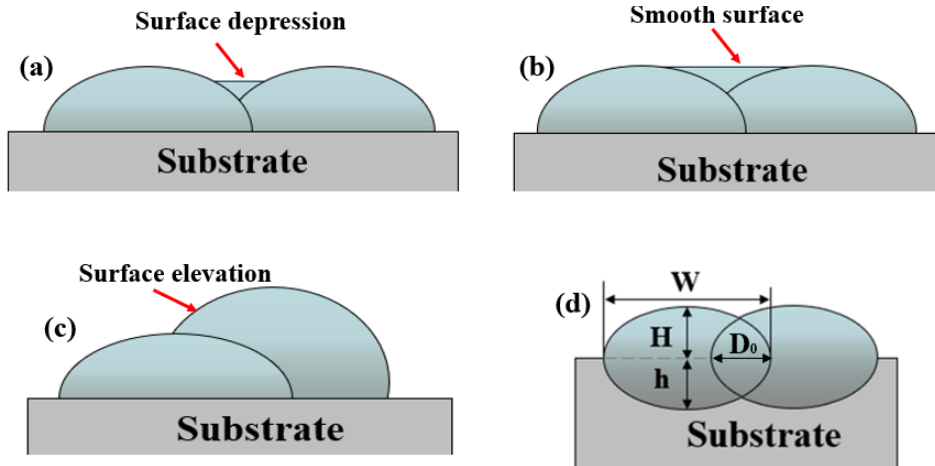


Fig. 3. A sketch of the effect of different overlap rates on the cross-section morphology of the cladding layer: (a) morphology of the cladding layer with too low an overlap rate; (b) morphology of the cladding layer with a moderate overlap rate; (c) morphology of the cladding layer with too high an overlap rate; (d) schematic diagram of the calculation of the overlap rate of the cladding layer

Table 3. Experimental process parameters

Spindle speed (r/min)	Feed rate (mm/z)	Depth of cut (mm)
12000	0.004	0.65

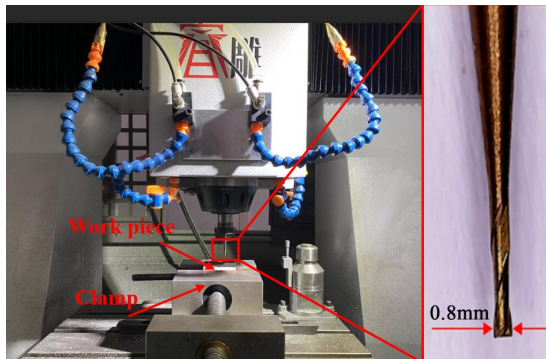


Fig. 4. Cutting test system

Yingpu Precision Industry Co Ltd. Machining parameters are shown in Table 3. As shown in Figure 4, the finished material is cleaned with an ultrasonic cleaner to remove surface debris and other impurities.

2.4. Characterization of the process

The machined surface was observed by the MR5000 inverted metallographic microscope and

the Sigma500 scanning electron microscope. Aztec X-Max 50 energy spectrometer was used to detect the element distribution. The surface morphology was characterized by a HYBRID C3 real color confocal microscope, and the roughness was calculated. The composition of the material image was observed by the D/Max-2500/PC X-ray diffractometer. The hardness of the material was measured by an HVS-1000 digital microhardness tester with a diamond probe.

3. Experimental results and discussion

3.1. The influence of different overlap rates on the morphology, microstructure, and properties of multi-pass laser cladding

Figure 5 shows the macroscopic and 3D real surface morphology of the laser cladding layer with different overlap rates. It can be seen that the surface of the cladding layer is smooth, and if there is no big porosity or crack, the experimental effect is better. As predicted before, when the overlap rate is 30%, the morphology of the cladding layer is “wavy,” which proves that the overlap rate is too low, and the channel gap is large. When the overlap rate is 70%, the protruding circle can be seen on

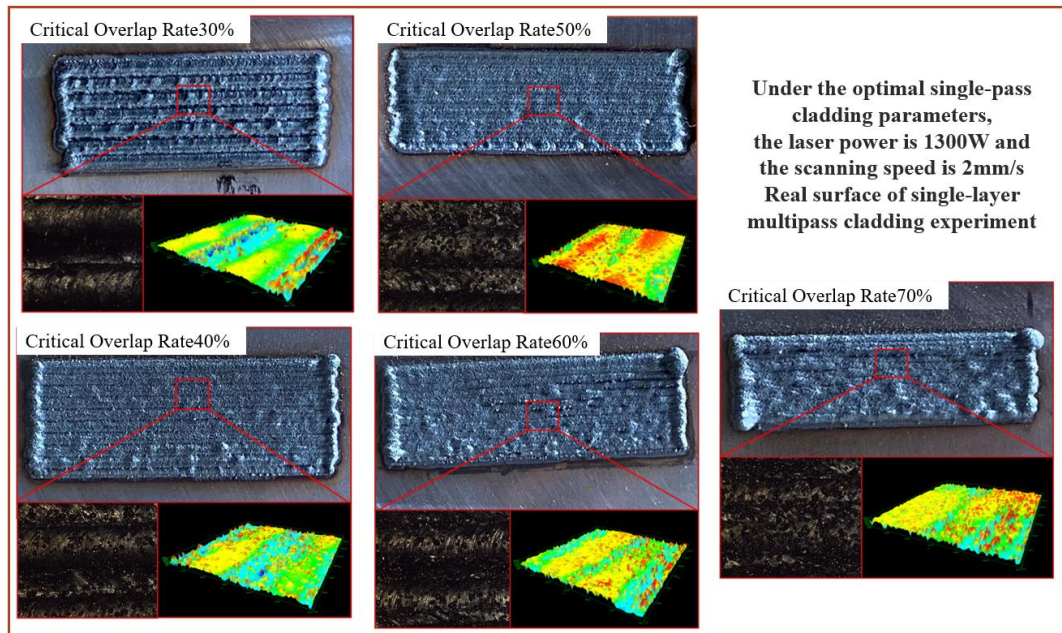


Fig. 5. Macroscopical morphology and three-dimensional real surface morphology of the cladding layer with different overlap rate

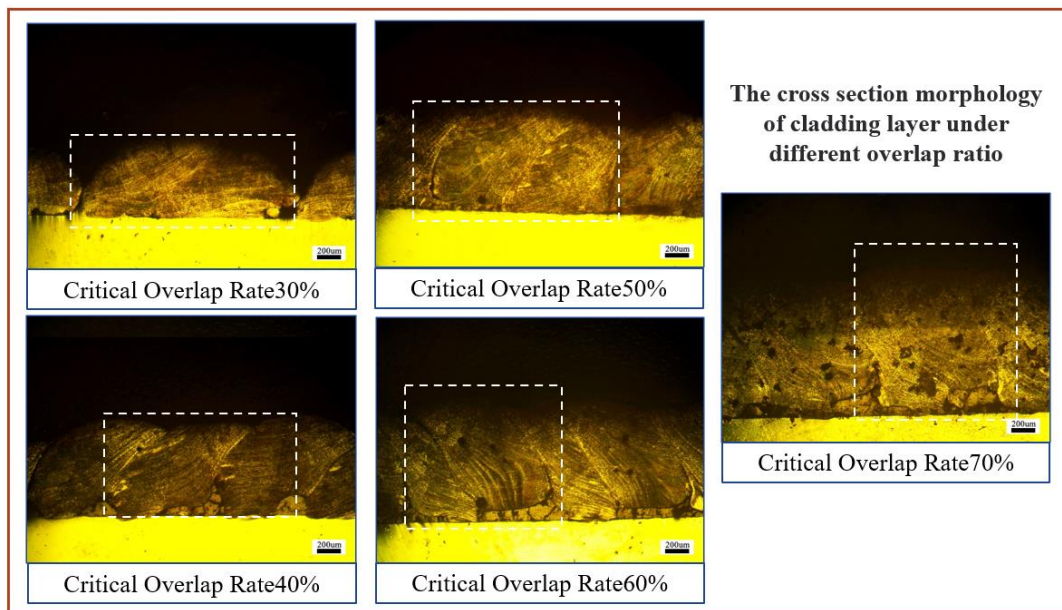


Fig. 6. Cross-section topography of cladding layer with different overlap rate

the surface of the cladding layer, which proves that the overlap of the cladding layer is caused by the high overlap rate. When the lap rate is 40% to 60%, although there will be a “wavy” morphology and cladding overlap, it will not be obvious.

Figure 6 shows the section morphology of the cladding layer under a different overlap rates. It can further be seen from the figure that the cladding layer section is wavy when the overlap rate is 30%, some of the incompletely melted powder

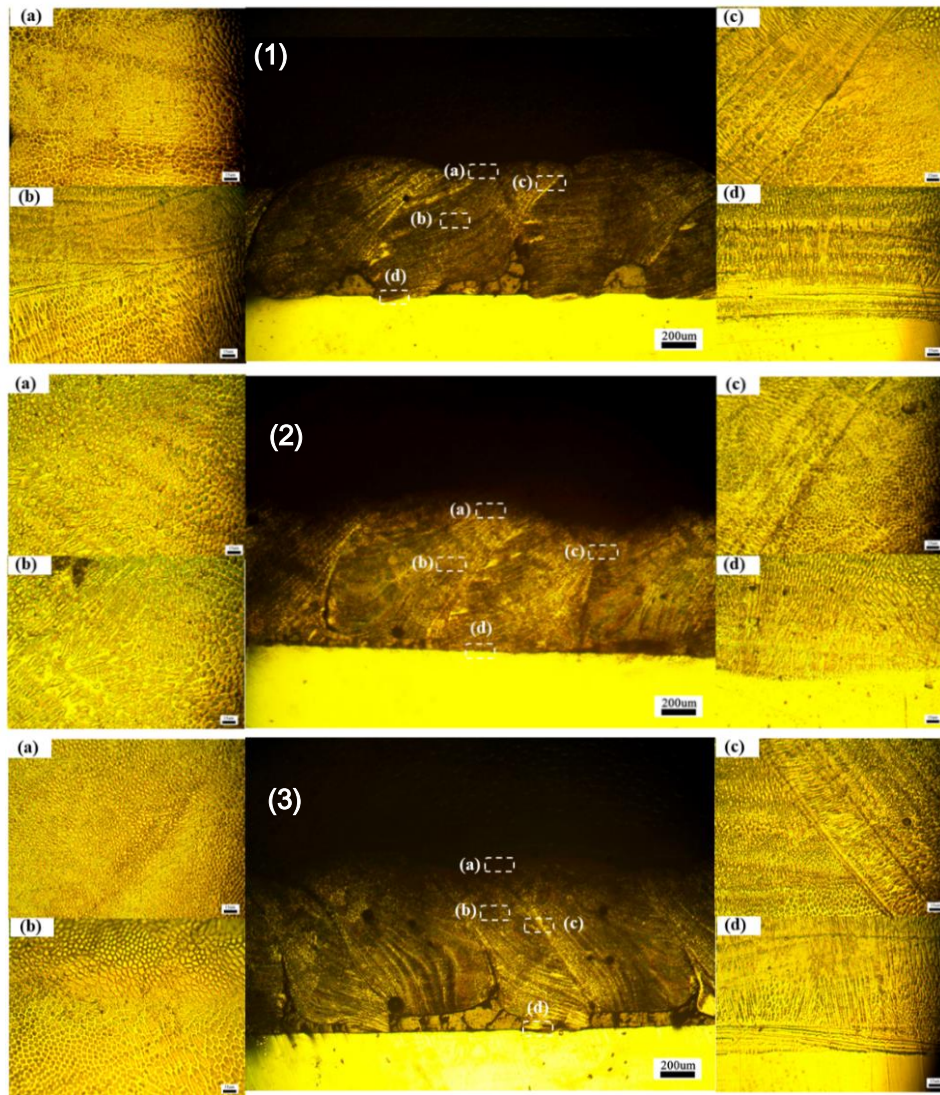


Fig. 7. Metallographic structure of cladding layer at different positions under different overlap rates: (1) overlap rate 40%; (2) overlap rate 50%; (3) overlap rate 60%

will be retained. This results in nonfusion defects, which can lead to stress concentration and crack initiation [23, 24]. When the overlap rate is 70%, it is obvious that the height of the cladding layer is higher than the other overlap rates, and the height difference of the cladding layer is obvious. When overlap occurs, there is a big gap between the base material and the bottom of the cladding layer, and the bonding effect is not good. When the overlap rate is 40% to 60%, the lapping effect is good, and there is no obvious crack or overlapping part in the adjacent melt path. When combined

with the macro-morphology and three-dimensional real surface morphology of the cladding layer, the lapping effect is not good when the overlap rate is 30% and 70%, so it is not considered. The analysis is continued when the overlap rate is 40% to 60%.

Figure 7 shows the metallographic structure of the cladding layer at different positions in the cross-section of the laser cladding experiment under the overlap rate of 40%, 50% and 60%. (a) shows the metallographic structure at the top of the cladding layer, (b) shows the metallographic structure at the middle of the cladding layer,

(c) shows the microstructure at the lap of the cladding layer, (d) shows the microstructure at the bottom of the cladding layer, and the microstructure evolution is mainly determined by the ratio of a temperature gradient to solidification rate [25]. The metallographic structure at (a) consists of fine cellular and equiaxed crystals because of the large area of heat exchange between the top of the cladding layer and the outside during fabrication, resulting in smaller and denser crystals [26]. The microstructure at (b) is composed of columnar dendrites and a small number of cellular crystals. As a result of the high cooling rate, uneven temperature distribution, and thermal diffusion of the molten pool, some of the columnar dendrites were biased or even stopped growing. The reason why the dendrites are clustered and directional is that the distance between adjacent melt paths is close during laser cladding, and some materials will have secondary crystallization during lapping. The growth direction of columnar dendrites is changed, and these crystals grow in the direction of the previous coating surface, that is, in a negative direction along a temperature gradient [27]. The microstructure at (c) is composed of columnar dendrites with different orientations and mixed cellular crystals along the arc of the lapping surface. Due to the different temperatures at different positions on the lapped surface, during the next lapping process, the second laser heat input and the residual heat on the lapped surface act together, making the heat flow direction at different positions on the lapped surface different, influencing the direction of dendrite growth [28]. The interlaced dendrite growth is also beneficial to prevent the crack from forming through the whole cladding layer when the thermal stress is too high in the laser cladding experiment. The microstructure of (d) is composed of columnar dendrites growing perpendicular to the fusion line and mixed with cellular crystals. Because of the decrease of heat input at the bottom of the molten pool, the temperature gradient increases, and the solidification rate is small. Therefore, the temperature gradient is larger than the solidification rate, and the crystallization of the cladding layer grows in a dendritic manner with fine crystal structure interspersed between them. An obvious curve

appears at the interface between the cladding layer and the substrate, which is the boundary between the cladding layer and the substrate. It shows that there is a good metallurgical effect between the cladding layer and the substrate.

The metallographic structure of the cladding layer at different positions in the laser cladding experiment under the overlap rate of 40%, 50%, and 60% was compared. When the overlap rate is 40%, the bonding porosity between the cladding layer and the substrate is larger, which is caused by an overlap rate that is too small and gap between melt paths that is too wide. When the overlap rate is 50%, the bonding between the cladding layer and the substrate is better, the microstructure is distributed evenly, and there is no obvious defect. The microstructure at the top of the cladding layer is smaller when the overlap rate is 60%, but the grain size of the other parts is larger because there are more overlapping parts between the melt paths. This leads to the growth of the grain of the other parts, and, finally, the coarse grains are formed. The results show that the microstructure of the cladding layer is the same in the same area under conditions of different overlap rates, and the change in overlap rate has no effect on the microstructure.

Figure 8 shows the metallurgical bonding zone at the bottom of the cladding layer by EDS scanning at the rates of 40%, 50%, and 60%. As can be seen from the diagram, the metallurgical bonding zone at the bottom of the cladding layer is continuous and compact, without obvious cracks and gaps. The element distribution in the metallurgical bonding zone at the bottom of the cladding layer was observed, and the distribution of the elements is consistent at each overlap rate. Fe is the main element. By scanning from the substrate to the cladding layer, it was found that Cr decreased to a stable trend, and Ni increased to a stable trend, which proved that the elements exchanged at the junction between the substrate and the cladding layer, which constitutes a good metallurgical effect.

Figure 9 is the SEM micrograph of the top of the cladding layer under the overlap rate of 40%, 50%, and 60%. Panels a, b, and c are observed under 1k magnification; panels a1, b1, and c1 are observed under 3k magnification. It can be

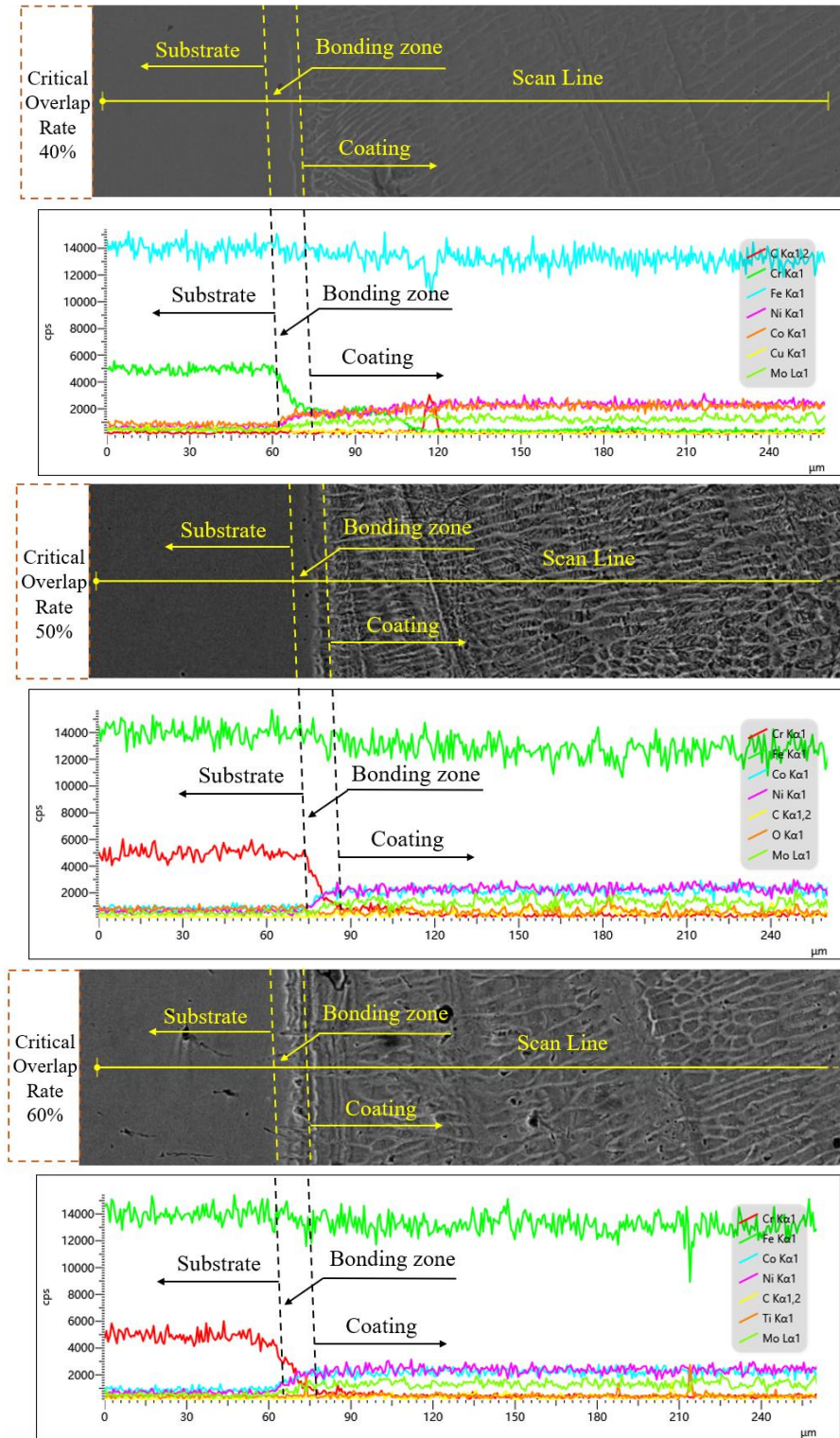


Fig. 8. The scanning result of the metallurgical bonding zone at the bottom of the cladding layer under conditions of different overlap rates

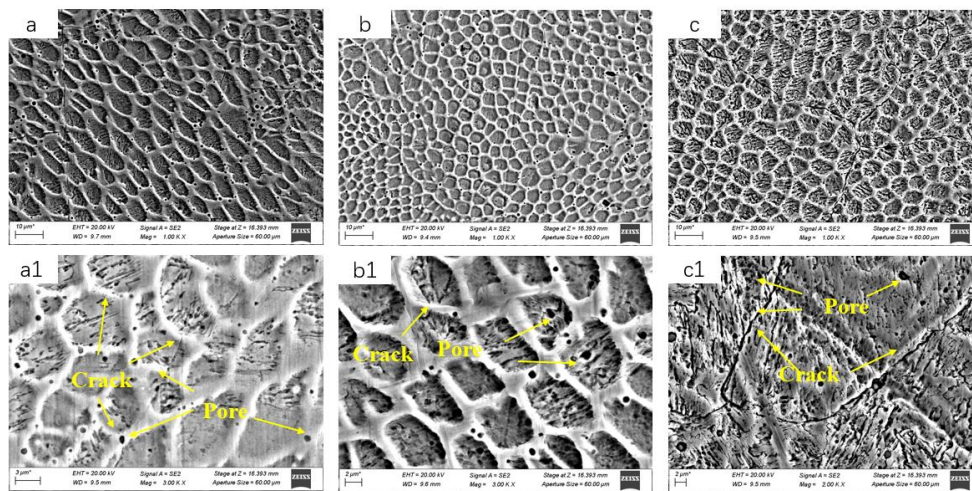


Fig. 9. The top microstructure of the cladding layer under different overlap rates: the overlap rate of a and a1 is 40%; that of b and b1 is 50%; and that of c and c1 is 60%

seen from the diagram that the microstructure of each lap rate consists of rough martensite with uniform distribution and obvious grain boundaries. The microstructure morphology of the cladding layer is the same as that of the 18Ni300 made by Chaolin Tan additive [29]. Under a 3k magnifying mirror, it can clearly be seen that there are pores and short cracks on the surface when the overlap rate is 40% and 50%. There are penetrating cracks when the overlap rate is 60%: the crack length is long and the crack width is large. At the same time, many branches are extending in other directions at the end of the crack, which may be due to the large residual stress of surface compression when the overlap rate is too high [30], which leads to the increase of the crack growth rate [31, 32], thus producing a larger crack.

Figure 10 shows the SEM-EDS map of the overlap of the cladding layer under 40%, 50%, and 60% laser cladding experiments. Table 4 shows the content of elements under each overlap rate. According to the content of each element (shown in Table 3), it can be seen that the distribution and content of the five elements are approximately the same: the content of Fe is the highest, followed by Ni, Co, MO, and C. The microstructure of the lapped joint is small and grows alternately along the forming direction, because the microstructure of the lapped joint is optimized by laser remelting.

The columnar crystal and nonequilibrium structure are eliminated, resulting in finer and more uniform grain morphology and distribution [33]. A few pores and short cracks occur at a 40% overlap rate, the microstructure morphology is good at a 50% overlap rate without obvious defects, and the microstructure morphology is very bad at a 60% overlap rate, when a large number of through-through cracks occur at the top of the microstructure of the cladding layer.

Figure 11 shows the hardness curves of the cladding layer under conditions of 40%, 50%, and 60% overlap rates. The hardness values were measured from the top of the cladding layer, with a load of 100 g applied to each measurement, and an interval of 0.15 mm, for a total of 17 measurements. It can be seen from the figure that the hardness of each overlap rate changes following the same trend: the hardness of the cladding layer is higher than that of the substrate due to the different preparation technology of the substrate and the cladding layer. The smaller the grain size, the larger the area of grain boundary; and the stronger the bonding force between metals, the higher the hardness and the higher the mechanical properties of the material [34]. In conclusion, the hardness of the lap joint has an increasing trend [35–37], there is an upward trend in the hardness of the lap region because of the its secondary processing [38]: the

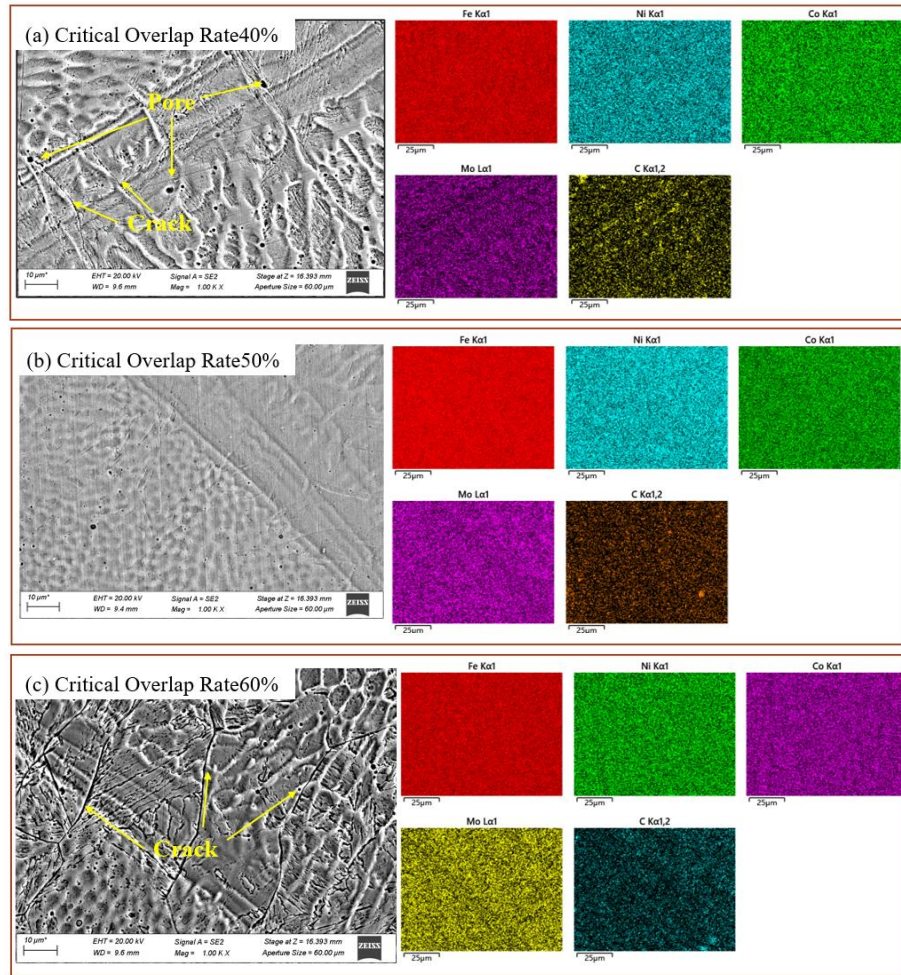


Fig. 10. SEM-EDS map of the lap joint of the cladding layer under differing overlap rates

Table 4. The content of each element in 40%, 50%, and 60% EDS mapping

Overlap rate	Fe	Ni	Co	Mo	C
40%	62.52	16.28	8.76	4.65	7.8
50%	62.72	16.45	8.90	4.45	7.48
60%	61.20	16.23	8.30	4.26	10.01

grains are refined and the distance between grains is reduced, the dislocation movement was significantly inhibited, and the hardness and strength were increased [39]. The average hardness of 50% is higher than that of 40% and 60% because of the cracks and pores in the additive manufacturing. Based on the above analysis, the cladding effect is best when an overlap rate is 50%. The cladding layer with an overlap rate of 50% is processed.

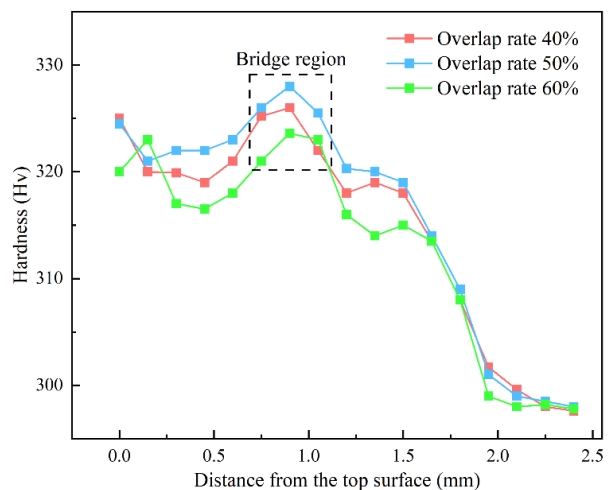


Fig. 11. Microhardness of the cladding layer under different overlap rates

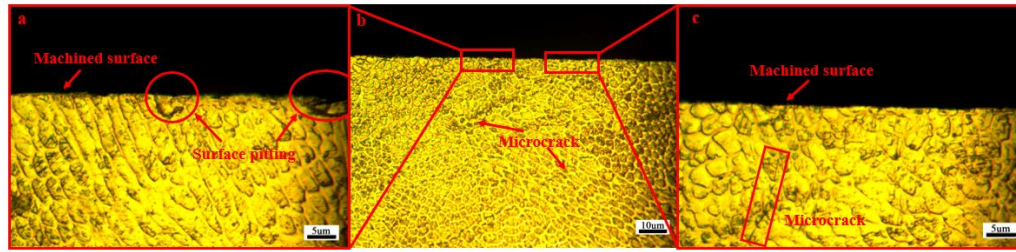


Fig. 12. Surface profile of cladding layer with 50% overlap after milling: (a) crater defects on the milled surface; (b) milled surface; (c) crack defects on the milled surface

3.2. The cutting surface quality of multi-pass laser cladding

Milling experiments were conducted on cladding parts with 50% overlap rate, Figure 12 shows the surface section morphology after milling. It can be seen from the figure that the milled surface of the additive material is very smooth without major defects, and, in contrast with Figure 7(2), the distortion and tensile deformation of the grains of the metallographic structure are very small. It may be that the smaller the depth of cutting and the smaller the diameter of the tool, the smaller the deformation. As can be seen from Figure 12(a), small pits appear after the cutting surface because the cladding layer contains some small, unmelted particles mixed into it, which fracture when the particles come into contact with the tool under maximum stress. Some of the particles remain bonded to the matrix, and some are pulled out entirely, causing the cutting surface to sag. As can be seen from Figure 12(c), during milling, the material of the workpiece undergoes elastic and plastic deformation with the local temperature rising, and induced milling surface residual stress has a new effect on the workpiece surface [40–42], resulting in small cracks.

Figure 13 shows the surface morphology after milling at a 50% overlap rate. Panel a is the surface after milling under a metallographic microscope, panel b is the true surface morphology, and panel c is the macroscopic surface after milling. From Figure 13a, we can see that there is a small defect on the surface: the friction in the contact area after milling increases, resulting in an increasing cutting force and cutting temperature. The increased

plastic flow ability of the workpiece results in plastic flow defects (Fig. 13a Mark I), pores in the cladding experiment (Fig. 13a Mark II), micro-cracks in the cladding experiment (Fig. 13a Mark III), scratches on the cutting surface caused by forward milling of some chips or unmelted powder (Fig. 13a Mark IV), and pits formed when the bulk of the cladding surface is removed (Fig. 13a Mark V). After milling, the surface of the workpiece is smooth. The surface roughness of Figure 13b was measured to be $0.342 \mu\text{m}$. The improved surface quality after milling is convenient for subsequent use [43].

Scanning electron microscopy of the milled surface is shown in Figure 14, with burrs growing unevenly along the cut direction of the channel [44]. From Fig. 14(a), it can be seen that the fine chips pushed out by the milling side are scattered at the top to form long whiskers, occasionally forming large burrs with continuous curls. From Figure 14(b), it can be seen that the side burr of reverse milling is large and has a continuously wavy shape, while the action mode between tool and workpiece material is mainly extrusion, friction, and plow effect. The burr on the reverse milling side is larger than that on the down milling side, and the shape of the burr is irregular. The burr is more complicated because the continuous advance of the milling cutter results in the wear of the carbide cutter and an increase in the radius of the cutter tip. The tool extrudes from the side of the workpiece, some material moves to the upper surface under the condition of plastic deformation, and some chips are removed on the down milling side. Most material enters the cutting end along the rake face, bending and fractures then occur

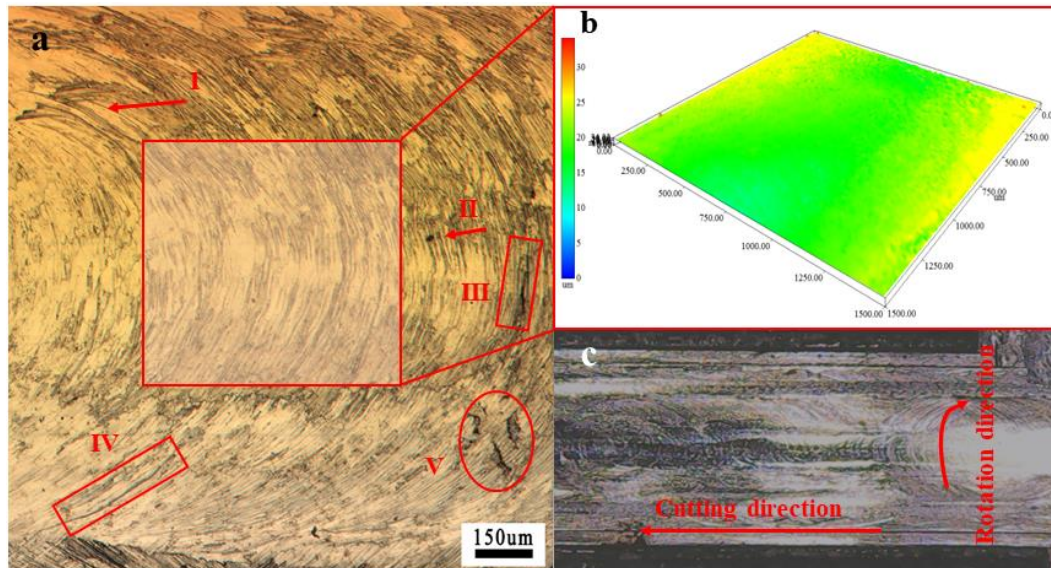


Fig. 13. Surface morphology of cladding layer after milling with 50% overlap rate: (a) surface after milling under a metallographic microscope; (b) the true surface morphology; (c) macroscopic surface after milling

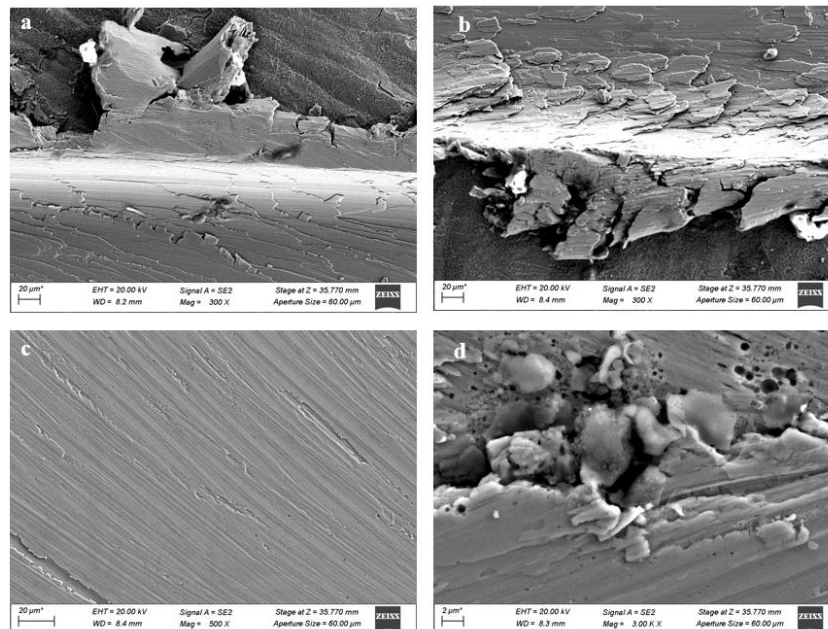


Fig. 14. SEM appearance of the milling surface of the cladding layer with 50% overlap: (a) down milling side burr topography, (b) reverse milling side burr appearance, (c) milling surface topography, and (d) milling surface defects

on the reverse milling side [45]. As a result, the burr on the reverse milling side is larger and more irregular. Compared to reverse milling, the down milling side is subjected to less impact, which results in smaller burrs and less impact on tool

wear [46]. A larger ratio of the cutting depth to the radius of the edge circle can be chosen in milling to reduce burrs [47]. Figure 14(c) is the milling surface topography, from which it can be seen that there are obvious tool marks on the surface, and

some parts of the surface have spalling, but the overall smoothness is good, with no large obvious defects. Figure 14(d) shows the defect of the cutting surface. It mainly involves the chopping of the air hole and the unmelted powder in the laser cladding. The laser power can be increased to melt the powder sufficiently in order to reduce the surface defect. Defects in additive manufacturing can also be avoided by varying the depth of the cut.

4. Conclusions

To sum up, the cladding experiments were carried out under different lap rates, and the resulting cladding layer morphology, microstructure, and hardness were analyzed to select the best overlap rate. According to the actual machining conditions in the factory, the surface of the additive manufacturing material is milled, and the cutting surface is analyzed. The conclusions are as follows:

- (1) Because of the difference in overlap rates, the morphology of the cladding layer mainly presents three phenomena: wave-like, flat-like, and overlap of the cladding layer. There are only a few lapped parts between the small melt paths, and the adjacent molten pool cannot fully combine. Some incompletely melted powder inevitably remains, and the unfused defects can easily cause stress concentration and crack initiation. If the overlap rate is too high, the overlap of the cladding layer can be seen, which results in a height that is greater than is produced by other overlap rates.
- (2) Under different overlap rates, the metallographic structure at the top of the cladding layer is composed of fine cellular and equiaxed crystals, and the metallographic structure in the middle of the cladding layer is composed of columnar dendrite and a few cellular crystals. The microstructure of the lapped layer is composed of columnar dendrite with a different orientation and with cellular crystal along the arc of the lapped surface. The microstructure at the bottom of

the cladding layer is composed of columnar dendrites growing perpendicular to the fusion line and mixed with cellular crystals. The results show that the metallographic structure of the cladding layer is the same in the same area under different overlap rates, and the change in overlap rate has no effect on the microstructure, but does have an effect on the size of the cladding layer.

- (3) Under high magnification, it can be clearly seen that there are pores and cracks on the surface when the overlap rate is 40% and 50%; there are penetrating cracks when the overlap rate is 60%, and this brings the possibility of new defects. The average hardness of the cladding layer is higher than that of the substrate hardness, and the hardness of the top of the cladding layer and the lap area is still higher. The effect of cladding is best when the overlap rate is 50%.
- (4) The materials produced by additive manufacturing have better milled surface smoothness and flatness; the measured surface roughness is $0.342 \mu\text{m}$. Milling surface defects include the following: plastic flow defects, pores, cracks, some chips or unmelted powder on the cutting surface which can leave scratches. The burrs are larger on the reverse-milling side than on the down-milling side.

Acknowledgements

This work was supported by Key Research and Development Program of Liaoning Province (2022JH1/10800022). All data included in this paper are available upon request through contact with the corresponding authors. The authors declare no conflict of interest.

Data Availability Statement: The data presented in this study are available upon request from the corresponding author.

Conflicts of Interest: The authors declare no conflict of interest.

References

- [1] Silva TEF, Rosa PAR, Reis AR, de Jesus AMP. Machinability of the 18Ni300 additively manufactured maraging steel based on orthogonal cutting tests. In: Machado J, Soares F, Trojanowska J, Ottaviano E, editors. *Innovations in mechanical engineering. Part of:*

- Lect. Notes Mech. Eng.* Singapore: Springer, 2022. doi: 10.1007/978-3-030-79165-0_1
- [2] Yang Z, Hao H, Gao Q, et al. Strengthening mechanism and high-temperature properties of H13+WC/Y2O3 laser-cladding coatings. *Surf Coat Technol.* 2021;405:126544. doi: 10.1016/j.surfcoat.2020.126544
- [3] Jiang Z, Sun J, Berto F, Wang X, et al. Fatigue and fracture behavior of AlSi10Mg manufactured by selective laser melting: a review. *Phys Mesomech.* 2023;26:367–90. doi: 10.1134/S102995992304001X
- [4] Wall A, Benoit JM. A review of existing solidification crack tests and analysis of their transferability to additive manufacturing. *J Mater Process Technol.* 2023;320:118090. doi: 10.1016/j.jmatprotec.2023.118090
- [5] Guiru M, Jingdong Z, Jiachen L, et al. Impact of pore defects on laser additive manufacturing of Inconel 718 alloy based on a novel finite element model: thermal and stress evaluation. *Opt Laser Technol.* 2023;167:109782. doi: 10.1016/j.optlastec.2023.109782
- [6] Zhao Y, Zhang H, Cai J, Sun X, et al. An efficient pores suppression process design method for high strength BCC high entropy alloys via powder bed fusion. *J Manuf Process.* 2023;101:371–85. doi: 10.1016/j.jmapro.2023.05.097
- [7] Bibin J, Manikandan M, Arivazhagan N, et al. Current research and developments in welding of 18% nickel maraging steel. *Proc Inst Mech Eng Pt L J Mater DesAppl.* 2023;237:1295–1318. doi: 10.1177/14644207221142516
- [8] Guo Q, Wang Y, Lin J. Effect of additive and subtractive hybrid manufacturing process on the surface quality of 18Ni300 maraging steel. *Mater Res Express.* 2023;10:056501. doi: 10.1088/2053-1591/acfe8
- [9] Hong S, Ha S, Song G, Cho J, et al. Correlation between micro-to-macro mechanical properties and processing parameters on additive manufactured 18Ni300 maraging steels. *J Alloys Compd.* 2023;960:171031. doi: 10.1016/j.jallcom.2023.171031
- [10] Yan L, Luo Q, He Z, Zhao H. Microstructure and mechanical properties of selective laser melted 18Ni300 steel. *Mater Sci-Poland.* 2022;40:64–71. doi: 10.2478/msp-2022-0031
- [11] Bai Y, Zhao C, Wang D, Wang H. Evolution mechanism of surface morphology and internal hole defect of 18Ni300 maraging steel fabricated by selective laser melting. *J Mater Process Technol.* 2022;299:117328. doi: 10.1016/j.jmatprotec.2021.117328
- [12] Mei X, Yan Y, Fu H, Gao X, Huang S, Qiao L. Effect of aging temperature on microstructure evolution and strengthening behavior of L-PBF 18Ni(300) maraging steel. *Addit. Manuf.* 2022;58:103071. doi: 10.1016/j.addma.2022.103071
- [13] Li JN, Gong SL, Liu KG, Qi WJ, Tian J, Shan FH. Formation mechanism and mechanical properties of the selective laser melting Ni/Co base alloy. *J Alloys Compd.* 2019;777:963–7. doi: 10.1016/j.jallcom.2018.10.343
- [14] Calignano F. Investigation of the accuracy and roughness in the laser powder bed fusion process. *Virtual Phys Prototyp.* 2018;13:97–104. doi: 10.1080/17452759.2018.1426368
- [15] Bozkurt YB, Kavasoğlu YS, Atik B, Kovacı H, Uzun Y, Çelik A. Comparison study of corrosion behavior for chitosan coated Ti6Al4V alloy produced by selective laser melting and forging. *Progr Org Coat.* 2023;182:107655. doi: 10.1016/j.porgcoat.2023.107655
- [16] Syed BAM, Naveed H, Farrukh SA, Muhammad TA, Azhar AK, Muhammad I, et al. Effect of laser surface remelting on microstructure, mechanical properties and tribological properties of metals and alloys: a review. *Opt Laser Technol.* 2023;165:109588. doi: 10.1016/j.optlastec.2023.109588
- [17] Dang L, He X, Tang D, Wu B, Li Y. A fatigue life posterior analysis approach for laser-directed energy deposition Ti-6Al-4V alloy based on pore-induced failures by kernel ridge. *Eng Fract Mech.* 2023;289:109433. doi: 10.1016/j.engfracmech.2023.109433
- [18] Yasa E, Deckers J, Kruth J-P. The investigation of the influence of laser re-melting on density, surface quality and microstructure of selective laser melting parts. *Rapid Prototyp J.* 2011;17:312–27. doi: 10.1108/13552541111156450
- [19] Guofu L, Yi L, Mengya C, et al. Numerical simulation and experimental study on flatness of inclined multipass cladding coating. *Surf Technol.* 2023;8:1–19. <https://link.cnki.net/urlid/50.1083.TG.20230815.0846.002>
- [20] Shao Y, Xu P, Tian J. Numerical simulation of the temperature and stress fields in Fe-based alloy coatings produced by wide-band laser cladding. *Met Sci Heat Treat.* 2021;63:327–33. doi: 10.1007/s11041-021-00690-w
- [21] Cui Z, Hu X, Dong S, et al. Numerical simulation and experimental study on residual stress in the curved surface forming of 12CrNi2 alloy steel by laser melting deposition. *Materials.* 2020;13:4316. doi: 10.3390/ma13194316
- [22] Tang H, Li R, Zhu H, et al. Microstructure and mechanical property of Al-Zn-Mg-Cu aluminum alloy substrate repaired by laser directed energy deposition with Al-Mg-Sc alloy powder. *Mater Sci Eng Powder Metall.* 2022;27:111–20. doi: 10.19976/j.cnki.43-1448/TF.2021101
- [23] Liu B, Kuai Z, Li Z, et al. Performance consistency of AlSi10Mg alloy manufactured by simulating multi laser beam selective laser melting (SLM): microstructures and mechanical properties. *Materials.* 2018;11:2354. doi: 10.3390/ma11122354
- [24] Gao Y, Hong Y, Yin L, et al. Ultrafast growth of high-quality monolayer WSe2 on Au. *Adv Mater.* 2017;29:1700990. doi: 10.1002/adma.201700990
- [25] Tan H, Luo Z, Li Y, et al. Effect of strengthening particles on the dry sliding wear behavior of Al2O3–M7C3/Fe metal matrix composite coatings

- produced by laser cladding. *Wear*. 2015;324–5:36–44. doi: 10.1016/j.wear.2014.11.023
- [26] Li Z, Chai L, Tang Y, et al. 316L stainless steel repaired layers by weld surfacing and laser cladding on a 27SiMn steel: a comparative study of microstructures, corrosion, hardness and wear performances. *J Mater Res Technol*. 2023;23:2043–2053. doi: 10.1016/j.jmrt.2023.01.162
- [27] Fang Z, Qi W, Li Z. Effect of laser cladding bonding rate on microstructure, wear resistance and corrosion resistance of 304 stainless steel CoCrW coating. *Mater Guide*. 2021;35:12123–9. doi: 10.11896/cldb.20040103
- [28] Cui J, Yu J, Cao Y, et al. Microstructure and properties of laser cladding layer of multi-channel lap cobalt base alloy. *Heat Treat Met*. 2020;45:41–5. doi: 10.13251/j.issn.0254-6051.2020.03.009
- [29] Tan C, Zhou K, Ma W, et al. Microstructural evolution, nanoprecipitation behavior and mechanical properties of selective laser melted high-performance grade 300 maraging steel. *Mater Des*. 2017;134:23–34. doi: 10.1016/j.matdes.2017.08.026
- [30] Xu G, Luo K, Dai F, et al. Effects of scanning path and overlapping rate on residual stress of 316L stainless steel blade subjected to massive laser shock peening treatment with square spots. *Appl Surf Sci*. 2019;481:1053–63. doi: 10.1016/j.apsusc.2019.03.093
- [31] Syed KA, Ahmad B, Guo H, et al. An experimental study of residual stress and direction-dependence of fatigue crack growth behaviour in as-built and stress-relieved selective-laser-melted Ti6Al4V. *Mater Sci Eng A*. 2019;755:246–57. doi: 10.1016/j.msea.2019.04.023
- [32] Leuders S, Thöne M, Riemer A, et al. On the mechanical behaviour of titanium alloy TiAl6V4 manufactured by selective laser melting: Fatigue resistance and crack growth performance. *Int J Fatigue*. 2013;48:300–7. doi: 10.1016/j.ijfatigue.2012.11.011
- [33] Yasa E, Kruth J. Microstructural investigation of selective laser melting 316L stainless steel parts exposed to laser re-melting. *Procedia Eng*. 2011;19:389–95. doi: 10.1016/j.proeng.2011.11.130
- [34] Ming C, Tao L, Bowen S, et al. Study on critical bonding rate and flatness of laser cladding on inclined matrix. *Appl Laser*. 2023;43:26–32. doi: 10.14128/j.cnki.al.20234303.026
- [35] Yasa E, Deckers J, Kruth J. The investigation of the influence of laser re-melting on density, surface quality and microstructure of selective laser melting parts. *Rapid Prototyp J*. 2011;17:312–27. doi: 10.1108/13552541111156450
- [36] Liu B, Li QB, Li Z. Selective laser remelting of an additive layer manufacturing process on AlSi10Mg. *Results Phys*. 2019;12:982–8. doi: 10.1016/j.rinp.2018.12.018
- [37] Qi P, Li B, Wang T, et al. Microstructure and properties of a novel ternary Ti–6Zr–xFe alloy for biomedical applications. *J Alloy Compd*. 2020;854:157119. doi: 10.1016/j.jallcom.2020.157119
- [38] Shubhadeep M, Kumar BS, Supriya B. Fascinating microstructural evolution during consolidation and remarkable hardening behaviour of micro alloyed Al–Cu–Ni alloys. *Adv Powder Technol*. 2023;34:104183. doi: 10.1016/j.apt.2023.104183
- [39] Tushar S, Visvalingam B, Thiruvengatam V, et al. Effect of post weld heat treatment on weld metal microstructure and hardness of HFCA-TIG welded ASTM-B670 high temperature alloy joints. *JALMES*. 2023;3:100025. doi: 10.1016/j.jalmes.2023.100025
- [40] Wang Q, Liu Z. Microhardness prediction based on a microstructure-sensitive flow stress model during high speed machining Ti-6Al-4V. *J Manuf Sci*. 2018;140:091003. doi: 10.1115/1.4039889
- [41] Heigel JC, Phan TQ, Fox JC, et al. Experimental investigation of residual stress and its impact on machining in hybrid additive/subtractive manufacturing. *Procedia Manuf*. 2018;26:929–94. doi: 10.1016/j.promfg.2018.07.120
- [42] Wang Z, Zhou J, Ren J, et al. Hybrid prediction model for residual stress profile induced by multi-axis milling Ti-6Al-4 V titanium alloy combined finite element with experiment. *Int J Adv Manuf Tech Technol*. 2023;126:4495–511. doi: 10.1007/s00170-023-11406-0
- [43] Guo Q, Wang Y, Lin J. Effect of additive and subtractive hybrid manufacturing process on the surface quality of 18Ni300 maraging steel. *Mater Res Express*. 2023;10:056501. doi: 10.1088/2053-1591/accefe8
- [44] Zhang X, Yu T, Wang W, et al. Improved analytical prediction of burr formation in micro end milling. *Int J Mech Sci*. 2019;151:461–70. doi: 10.1016/j.ijmecsci.2018.12.005
- [45] Zhang Y, Yang G, Li J, et al. Milling experiment of diamond-coated micro-milling cutter. *Chin J Mech Eng-EN*. 2020;31:1772–7. doi: 10.3969/j.issn.1004-132X.2020.15.002
- [46] Guifam U, Syed H, Mushtao K, et al. Analysis of burr formation in low speed micro milling of titanium alloy (Ti6Al4V). *Mech Sci*. 2018;9:231–43. doi: 10.5194/ms-9-231-2018
- [47] Bissacco G, Hansen H, Chiffre DL. Size effects on surface generation in micro milling of hardened tool steel. *CIRP Ann-Manuf Technol*. 2006;55:593–6. doi: 10.1016/S0007-8506(07)60490-9

Received 2023-09-13

Accepted 2023-10-21